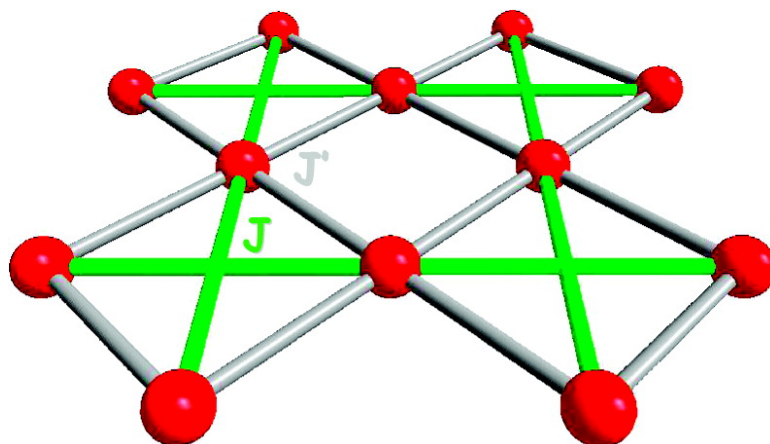


Structure and Magnetic Properties of Oxychalcogenides $A\text{FeOQ}$ ($A = \text{Sr}, \text{Ba}$; $Q = \text{S}, \text{Se}$) with FeO Square Planar Layers Representing an Antiferromagnetic Checkerboard Spin Lattice

Houria Kabbour, Etienne Janod, Benoit Corraze, Michel Danot,
Changhoon Lee, Myung-Hwan Whangbo, and Laurent Cario

J. Am. Chem. Soc., **2008**, 130 (26), 8261-8270 • DOI: 10.1021/ja711139g • Publication Date (Web): 06 June 2008

Downloaded from <http://pubs.acs.org> on February 8, 2009



More About This Article

Additional resources and features associated with this article are available within the HTML version:

- Supporting Information
- Links to the 2 articles that cite this article, as of the time of this article download
- Access to high resolution figures
- Links to articles and content related to this article
- Copyright permission to reproduce figures and/or text from this article

[View the Full Text HTML](#)

Structure and Magnetic Properties of Oxychalcogenides $A_2F_2Fe_2OQ_2$ ($A = Sr, Ba; Q = S, Se$) with Fe_2O Square Planar Layers Representing an Antiferromagnetic Checkerboard Spin Lattice

Houria Kabbour,[†] Etienne Janod,[†] Benoît Corraze,[†] Michel Danot,[†]
Changhoon Lee,[‡] Myung-Hwan Whangbo,[‡] and Laurent Cario^{*†}

Institut des Matériaux Jean Rouxel, CNRS-Université de Nantes, 2 rue de la Houssinière, BP32229, 44322 Nantes, France, and Department of Chemistry, North Carolina State University, Raleigh, North Carolina 27695-8204

Received December 19, 2007; E-mail: Laurent.Cario@cnsr-immn.fr

Abstract: The oxychalcogenides $A_2F_2Fe_2OQ_2$ ($A = Sr, Ba; Q = S, Se$), which contain Fe_2O square planar layers of the anti- CuO_2 type, were predicted using a modular assembly of layered secondary building units and subsequently synthesized. The physical properties of these compounds were characterized using magnetic susceptibility, electrical resistivity, specific heat, ^{57}Fe Mössbauer, and powder neutron diffraction measurements and also by estimating their exchange interactions on the basis of first-principles density functional theory electronic structure calculations. These compounds are magnetic semiconductors that undergo a long-range antiferromagnetic ordering below 83.6–106.2 K, and their magnetic properties are well-described by a two-dimensional Ising model. The dominant antiferromagnetic spin exchange interaction between $S = 2 Fe^{2+}$ ions occurs through corner-sharing $Fe-O-Fe$ bridges. Moreover, the calculated spin exchange interactions show that the $A_2F_2Fe_2OQ_2$ ($A = Sr, Ba; Q = S, Se$) compounds represent a rare example of a frustrated antiferromagnetic checkerboard lattice.

1. Introduction

Low-dimensional compounds of transition-metal elements have been extensively studied and still attract much interest because of their interesting electrical and magnetic properties. Binary transition-metal compounds with polarizable anions, such as transition-metal chalcogenides, are commonly found to have layered structures.¹ Addition of a second metal element requiring a different coordination environment often reinforces the tendency toward a layered structure. Numerous alkaline-earth or rare-earth transition-metal compounds exhibit layered-type intergrowth structures in which the two different cations are segregated into well-defined layers; examples include superconducting cuprates,² manganites with colossal magnetoresistance,³ thermoelectric misfit oxide cobaltites,⁴ and misfit chalcogenides,^{5–9} to name a few. The tendency toward the segregation is further promoted by the coexistence of two

different anions. A large number of rare-earth or alkaline-earth transition-metal oxychalcogenides^{10–13} and oxypnictides reported to date exhibit layered-type intergrowth structures.^{14,15} During the last three years, new inorganic compounds with intergrowth structures have been prepared by employing two-dimensional (2D) secondary building units (SBUs) and exploiting the tendency of mixed-anion systems to form layered-type intergrowth structures.¹⁶ As depicted in Figure 1, the structures of a whole family of compounds can be predicted from the stacking of 2D SBUs of the fluorite type $\{[A_2F_2]\}$ ($A = \text{alkaline earth}$) alternating regularly with 2D SBUs of the rock-salt $\{[M_nQ_{n+2}]\}$ ($M = \text{metal}; Q = \text{chalcogenide, pnictide}$) or anti-fluorite $\{[M_2Q_2]\}$ type.^{17–19} In essence, the 2D SBUs were found to keep their structural and electronic properties after being assembled together.¹⁹ This feature led to the prediction of new

[†] CNRS-Université de Nantes.

[‡] North Carolina State University.

(1) Jobic, S.; Brec, R.; Rouxel, J. *J. Alloys Compd.* **1992**, *178*, 253.

(2) Wong-ng, W. K.; Davis, K. L.; Roth, R. S. *J. Am. Ceram. Soc.* **1988**, *71*, C64.

(3) Kimura, T.; Tokura, Y. *Annu. Rev. Mater. Sci.* **2000**, *30*, 451.

(4) Maignan, A.; Hebert, S.; Pi, L.; Pelloquin, D.; Martin, C.; Michel, C.; Hervieu, M.; Raveau, B. *Cryst. Eng.* **2002**, *5*, 365–382.

(5) Wiegers, G. A.; Meerschaut, A. In *Incommensurate Sandwiched Layered Compounds*; Meerschaut, A., Ed.; Trans Tech Publications: Zurich, 1992; pp 101.

(6) Cario, L.; Corraze, B.; Meerschaut, A.; Chauvet, O. *Phys. Rev. B* **2006**, *73*, 155116.

(7) Cario, L.; Meerschaut, A.; Corraze, B.; Chauvet, O. *Mater. Res. Bull.* **2005**, *40*, 125.

(8) Cario, L.; Palvadeau, P.; Lafond, A.; Deudon, C.; Moelo, Y.; Corraze, B.; Meerschaut, A. *Chem. Mater.* **2003**, *15*, 943.

(9) Cario, L.; Lafond, A.; Palvadeau, P.; Deudon, C.; Meerschaut, A. *J. Solid State Chem.* **1999**, *147*, 58.

(10) Goga, M.; Seshadri, R.; Ksenofontov, V.; Gütllich, P.; Tremel, W. *Chem. Commun.* **1999**, 979.

(11) Boyer, C.; Deudon, C.; Meerschaut, A. *C. R. Acad. Sci. Paris* **1999**, *93*.

(12) Otszchi, K.; Ogino, H.; Shimoyama, J. I.; Kishio, K. *J. Low Temp. Phys.* **1999**, *117*, 729.

(13) Cario, L.; Popa, A. F.; Lafond, A.; Guillot-Deudon, C.; Kabbour, H.; Meerschaut, A.; Clarke, S. J.; Adamson, P. *Inorg. Chem.* **2007**, *46*, 9584.

(14) Ozawa, T. C.; Kauzlarich, S. M.; Bieringer, M.; Wiebe, C. R.; Greedan, J. E.; Gardner, J. S. *Chem. Mater.* **2001**, *13*, 973.

(15) Nientiedt, A. T.; Jeitschko, W. *Inorg. Chem.* **1998**, *37*, 386.

(16) Cario, L.; Kabbour, H.; Meerschaut, A. *Chem. Mater.* **2005**, *17*, 234.

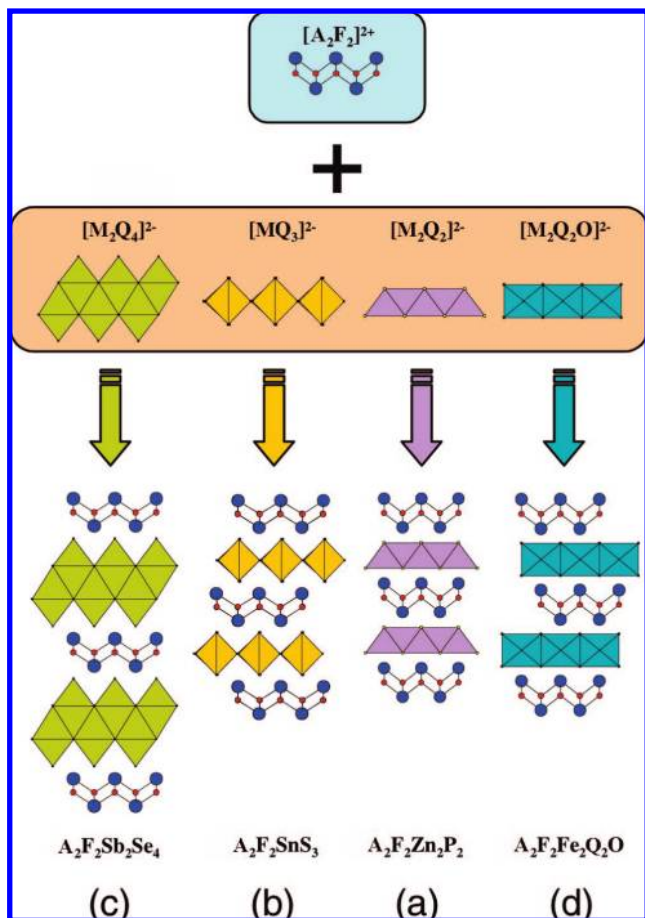


Figure 1. Illustration of the prediction of different families of compounds using the concept of layered 2D SBUs. All of the compounds contain similar donor 2D SBUs of the fluorite type ($[A_2F_2]^{2+}$). The AFZnP compounds (a) were the first compounds predicted using acceptor anti-fluorite ($[M_2Q_2]^{2-}$) 2D SBUs. More-complex acceptor 2D SBUs of the NaCl type ($[M_nQ_{n+2}]^{2-}$) were then used, leading to the prediction of the homologous series $A_2F_2M_nQ_{n+2}$ containing compounds such as (b) $Ba_2F_2SnS_3$ ($n = 1$) and (c) $SrF_2Sb_2Se_2$ ($n = 2$). The final step (d) of this strategy, which has been implemented in the present work, was to use 2D SBUs of the form $[Fe_2OQ_2]$, which contain Fe_2O square planes that are inclined to present interesting physical properties.

compounds with targeted properties, e.g., p-type transparent conductors.²⁰

Oxides and oxychalcogenides of transition-metal elements that contain CuO_2 -type square planar layers exhibit a variety of physical properties, such as superconductivity, colossal magnetoresistance, and metamagnetism. In contrast, compounds with anti- CuO_2 -type square planar layers are rare and also attractive since they may exhibit interesting physical properties. To our knowledge, such anti- CuO_2 -type layers have been found to occur exclusively in the mixed-anion systems $Na_2Ti_2Sb_2O$,^{21,22} $Na_{1.9}Cu_2Se_2Cu_2O$,²³ and $La_2O_2-Fe_2OSe_2$.²⁴ $Na_{1.9}Cu_2Se_2Cu_2O$ is a metallic compound with p-type conduction induced in the $[Cu_2Se_2]$ layer by vacancies of Na^+ ions. $Na_2Ti_2Sb_2O$ has been the subject of numerous

Table 1. Atomic Coordinates for the Hypothetical AFM Structure of $Ba_2F_2Fe_2OSe_2$ (Space Group $P4_2/mmc$, $a = 4.187 \text{ \AA}$, $c = 19.820 \text{ \AA}$)

atom	site	x	y	z
Ba	4i	$1/2$	0	0.1685
Fe1	2a	0	0	$1/2$
Fe2	2b	$1/2$	$1/2$	0
Se	4i	0	$1/2$	0.0876
F1	2e	0	0	$3/4$
F2	2f	$1/2$	$1/2$	$1/4$
O	2d	$1/2$	0	0

studies because of its charge-density-wave-like behavior, but only a few studies have been reported for $La_2O_2Fe_2OSe_2$. In the present work, we have used the concept of 2D SBUs to predict a new family of oxychalcogenides, $A_2F_2Fe_2OQ_2$ ($A = Sr, Ba$; $Q = S, Se$), whose members contain Fe_2O square planar layers of the anti- CuO_2 type. We subsequently determined their crystal structures using X-ray diffraction and characterized their physical properties by performing electrical resistivity, magnetic susceptibility, specific heat, powder neutron diffraction, and Mössbauer spectroscopy measurements. Moreover, we also estimated the spin exchange interactions of these compounds on the basis of first-principles density functional theory (DFT) electronic structure calculations.

2. Experimental Section

First-principles DFT calculations were carried out with the Vienna ab-initio simulation package (VASP)²⁵ using the frozen-core projector-augmented-wave (PAW) method²⁶ and the generalized gradient approximations (GGA)²⁷ for the exchange and correlation corrections. For optimization of the cell parameters and atomic positions of $Ba_2F_2Fe_2OSe_2$ and $Sr_2F_2Fe_2OS_2$, we employed a plane-wave cutoff energy of 500 eV and 25 k points for the irreducible Brillouin zone. All of the structural optimizations converged with residual Hellman–Feynman forces on the atoms smaller than 0.03 eV/Å. Results are given in Table 1. To evaluate the spin exchange interactions, our calculations employed a plane-wave cutoff energy of 400 eV, 32 k points for the irreducible Brillouin zone, and a total-energy convergence threshold of 10^{-5} eV.

All of the compounds were synthesized by solid-state reaction. The starting materials AF_2 , AO , Fe , and Q were mixed in stoichiometric proportions and then pressed into pellets in a glove box. The mixture was placed in an evacuated silica tube, heated to 800 °C over 12 h (50 °C/h), and then cooled to room temperature (100 °C/h). For the selenide compounds, an initial heating step (220 °C for 12 h) was needed in order to obtain the pure phases. The mixtures were then ground again and reheated to the same temperature for 12 h. For $Ba_2F_2Fe_2OSe_2$ and $Sr_2F_2Fe_2OS_2$, a final heat treatment at 1000 °C led to congruent fusion and subsequent growth of crystals.

Chemical analyses of all of the compounds were performed on powder or crystal samples using an electron microscope (JEOL 5800LV) equipped with an energy-dispersive X-ray spectroscopy (EDXS) apparatus. The presence of fluorine and oxygen was

- (17) Kabbour, H.; Cario, L.; Danot, M.; Meerschaut, A. *Inorg. Chem.* **2006**, *45*, 917.
 (18) Kabbour, H.; Cario, L. *Inorg. Chem.* **2006**, *45*, 2713.
 (19) Kabbour, H.; Cario, L.; Boucher, F. *J. Mat. Chem.* **2005**, *15*, 3525.
 (20) Kabbour, H.; Cario, L.; Jobic, S.; Corraze, B. *J. Mater. Chem.* **2006**, *16*, 4165.
 (21) Adam, A.; Schuster, H. U. *Z. Anorg. Allg. Chem.* **1990**, *584*, 150.
 (22) Ozawa, T. C.; Kauzlarich, S. M. *Chem. Mater.* **2001**, *13*, 1804.

- (23) Park, Y.; DeGroot, D. C.; Schindler, J. L.; Kannewurf, C. R.; Kanatzidis, M. G. *Chem. Mater.* **1993**, *5*, 8.
 (24) Mayer, J. M.; Schneemeyer, L. F.; Siegrist, T.; Waszczak, J. V.; Van Dover, R. B. *Angew. Chem., Int. Ed. Engl.* **1992**, *31*, 1645.
 (25) Kresse G.; Furthmüller J. Vienna Ab-initio Simulation Package (VASP); Institut für Materialphysik: Vienna, 2004; <http://cms.mpi.univie.ac.at/vasp>.
 (26) Kresse, G.; Joubert, D. *Phys. Rev. B* **1999**, *59*, 1758.
 (27) Perdew, J. P.; Burke, S.; Ernzerhof, M. *Phys. Rev. Lett.* **1996**, *77*, 3865.

Table 2. EDXS Analysis Results (mol %) for $Ba_2F_2Fe_2OSe_2$, $Sr_2F_2Fe_2OS_2$, $Ba_2F_2Fe_2OS_2$, and $Sr_2F_2Fe_2OSe_2^a$

atom type	$Ba_2F_2Fe_2OSe_2$	$Sr_2F_2Fe_2OS_2$	$Ba_2F_2Fe_2OS_2$	$Sr_2F_2Fe_2OSe_2$
A	32.7	30.7	33.8	35.7
Fe	32.2	37.3	32.7	32.3
Q	35.1	32.0	33.5	32.0

^a For all three atom types, the theoretical value is 33.3 mol %, since the amounts of F and O could not be quantified.

Table 3. X-ray Data Collection and Structure Refinement Parameters for Single Crystals of $Ba_2F_2Fe_2OSe_2$ and $Sr_2F_2Fe_2OS_2$

	$Ba_2F_2Fe_2OSe_2$	$Sr_2F_2Fe_2OS_2$
Crystallographic and Physical Data		
molecular weight (g/mol)	598.30	405.06
symmetry	tetragonal	tetragonal
space group	$I4/mmm$	$I4/mmm$
<i>a</i> (Å)	4.1946(6)	4.0400(6)
<i>c</i> (Å)	19.522(4)	17.998(4)
<i>V</i> (Å ³)	343.49(10)	293.75(9)
<i>Z</i>	2	2
density (g/cm ³)	5.785	4.579
crystal dimensions (μm)	25 × 60 × 20	200 × 100 × 20
Data Collection and Reduction		
<i>T</i> (K)	293(2)	293(2)
λ (Å)	0.71073	0.71073
θ range (deg)	5.78–34.99	5.17–34.91
<i>h</i> , <i>k</i> , <i>l</i> ranges	−6 < <i>h</i> < 6, −6 < <i>k</i> < 6, −31 < <i>l</i> < 31	−6 < <i>h</i> < 6, −6 < <i>k</i> < 6, −28 < <i>l</i> < 16
collected reflections	3208	2305
independent reflections	270	233
observed reflections [<i>I</i> > 2σ(<i>I</i>)]	243	225
absorption correction	analytical	analytical
absorption coefficient (mm ^{−1})	25.990	23.544
<i>T</i> _{min} / <i>T</i> _{max}	0.339/0.614	0.077/0.588
<i>R</i> _{int}	0.0603	0.0483
Structural Refinement		
refinement method	least-squares on <i>F</i> ²	least-squares on <i>F</i> ²
<i>F</i> (000)	516	372
data/restraints/parameters	270/0/13	233/0/12
<i>R</i> (obs), <i>R</i> (all)	0.0196, 0.0233	0.0173, 0.0186
<i>R</i> _w (obs), <i>R</i> _w (all)	0.0421, 0.0436	0.0401, 0.0412
extinction coefficient	0.0097(8)	0.0229(18)
<i>S</i>	1.150	1.179
electronic residues (e/Å ³)	0.950, −1.487	1.52, −1.07

confirmed for all of the compounds, but their amounts could not be quantified because of experimental limitations. The EDXS results are presented in Table 2.

X-ray diffraction was performed on single crystals of $Ba_2F_2Fe_2OSe_2$ and $Sr_2F_2Fe_2OS_2$ mounted on capillaries. The X-ray data were collected on a Kappa CCD-NONIUS diffractometer using Mo K α radiation ($\lambda = 0.71073$ Å). The Gaussian analytical absorption correction was done by indexation of the crystal faces with respect to their dimensions. Secondary-extinction and Lorentz-polarization effects were also taken into account. The initial sets of reflections were averaged according to the $I4/mmm$ point group. In both cases, the data revealed tetragonal symmetry with cell parameter values of $a \approx 4.1$ Å and $c \approx 18$ – 20 Å, and the systematic absences were consistent with space group $I4/mmm$. Structural refinement in space group $I4/mmm$ using the predicted structure was performed with the program SHELXL.²⁸ Details concerning the single-crystal X-ray data collection and structure refinement procedures are gathered in Tables 3 and 4.

X-ray diffraction analyses of powder samples of $Ba_2F_2Fe_2OS_2$ and $Sr_2F_2Fe_2OSe_2$ were performed on a D5000 diffractometer using

(28) Sheldrick G. M. SHELXL97 University of Göttingen: Göttingen, Germany, 1997.

Table 4. Atomic Coordinates and Equivalent Isotropic Displacement Parameters (*U*_{iso}) for $Ba_2F_2Fe_2OSe_2$, $Sr_2F_2Fe_2OS_2$, $Sr_2F_2Fe_2OSe_2$, and $Ba_2F_2Fe_2OS_2$

atom	<i>x</i>	<i>y</i>	<i>z</i>	<i>U</i> _{iso} (Å ²)
$Ba_2F_2Fe_2OSe_2$				
Ba	1/2	1/2	0.16942(2)	0.00809(14)
Se	0	0	0.08982(3)	0.00756(15)
Fe	1/2	0	0	0.00889(17)
O	1/2	1/2	0	0.0086(10)
F	1/2	0	1/4	0.0107(6)
$Sr_2F_2Fe_2OS_2$				
Sr	1/2	1/2	0.17100(2)	0.00765(13)
S	0	0	0.09381(6)	0.00780(17)
Fe	1/2	0	0	0.00820(14)
O	1/2	1/2	0	0.0096(7)
F	1/2	0	1/4	0.0086(4)
$Sr_2F_2Fe_2OSe_2$				
Sr	1/2	1/2	0.1741(2)	0.037(2)
Se	0	0	0.0970(2)	0.042(2)
Fe	1/2	0	0	0.032(2)
O	1/2	1/2	0	0.010(10)
F	1/2	0	1/4	0.039(7)
$Ba_2F_2Fe_2OS_2$				
Ba	1/2	1/2	0.1659(2)	0.0434(14)
S	0	0	0.0871(5)	0.052(4)
Fe	1/2	0	0	0.040(3)
O	1/2	1/2	0	0.012(9)
F	1/2	0	1/4	0.040(9)

Table 5. Cell Parameters and Reliability Factors Obtained Using Rietveld Refinements of $Sr_2F_2Fe_2OSe_2$ and $Ba_2F_2Fe_2OS_2$ (Space Group $I4/mmm$)

	$Sr_2F_2Fe_2OSe_2$	$Ba_2F_2Fe_2OS_2$
<i>a</i> (Å)	4.0925(2)	4.1238(2)
<i>c</i> (Å)	18.5801(10)	19.0885(12)
<i>V</i> (Å ³)	311.20(3)	324.61(3)
<i>R</i> _{Bragg} (%)	3.96	5.82
<i>R</i> _{wp} (%)	1.57	3.20
<i>R</i> _p (%)	1.14	2.42
<i>R</i> _{exp} (%)	0.77	2.21
χ^2	4.57	2.25

Cu K α_1 and Cu K α_2 radiation ($\lambda \approx 1.542494$ Å). Data collection was performed at room temperature over a 2θ range of 10–110° with an acquisition time of 12 h. The cell parameters and the crystal structures were refined using the Rietveld method^{29,30} with the programs FullProf³¹ and WinPlotr.³² The background was fitted using linear interpolation between selected points. The March–Dollase model for preferred orientation was used in all of the refinements, and a pseudo-Voigt function was used as the peak-shape model. Details concerning the Rietveld refinements are gathered in Tables 4 and 5.

Electrical measurements were performed when single crystals were available (i.e., for $Ba_2F_2Fe_2OSe_2$ and $Sr_2F_2Fe_2OS_2$) using a four-probe method. The crystal dimensions were 300 μm. We used 20 μm gold wire electrodes that were attached to the sample using silver paste. The measurements were performed between 300 and 45 K at bias voltages smaller than 0.01 V.

Specific heat (*C*_p) measurements were performed in a homemade calorimeter using the semiadiabatic method. Data were recorded between 25 and 135 K on a pellet pasted with Apiezon N grease. A correction for the sample holder and grease was applied. Because

(29) Rietveld, H. M. *Acta Crystallogr.* **1967**, 22, 151.

(30) Rietveld, H. M. *J. Appl. Crystallogr.* **1969**, 2, 65.

(31) Rodríguez-Carvajal, J. *Int. Union Crystallogr. Newsl.* **2001**, 26, 12; FullProf is available for download at <http://www.ill.eu/sites/fullprof/>.

(32) Roisnel, T.; Rodríguez-Carvajal, J. *Mater. Sci. Forum* **2001**, 378–381, 118–123.

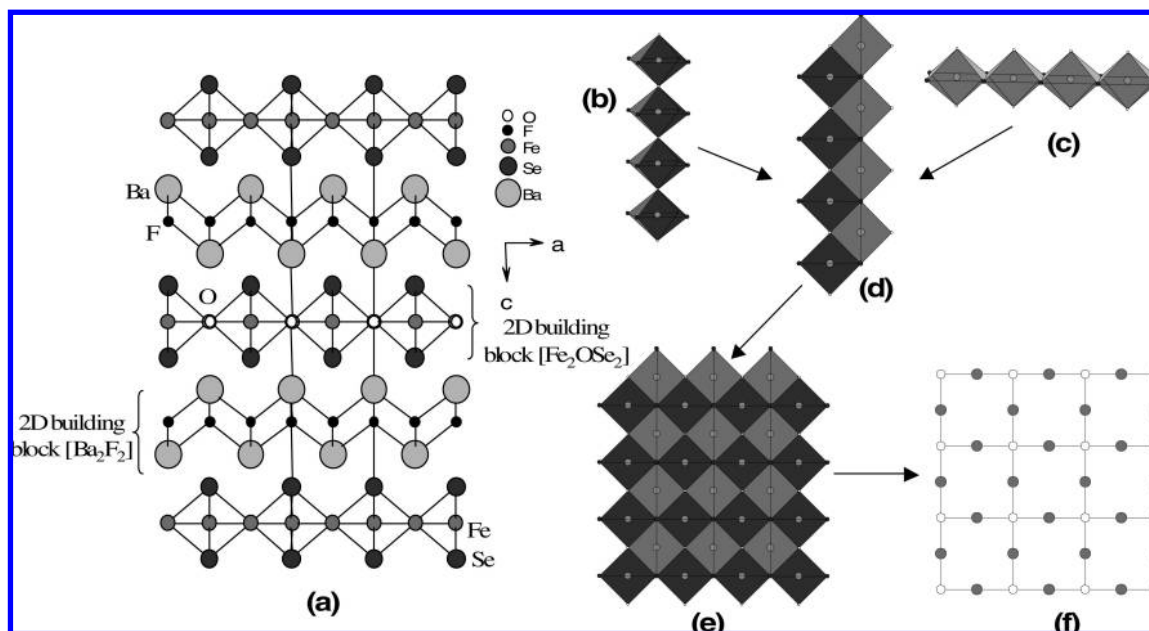


Figure 2. (a) Structure of the compounds $A_2F_2Fe_2OQ_2$ ($A = Sr, Ba$; $Q = S, Se$) and (e) description of the $[Fe_2OQ_2]^{2+}$ block as the combination of two chains of iron-centered octahedrons parallel to the ab plane: (b) the first chain consists of octahedrons linked together by corners, and (c) the second chain is formed by edge-connected octahedrons. (d) The two chains are joined by octahedron faces. In the Fe_4O_2 octahedrons, the equatorial planes are occupied by Q atoms while (f) the oxygen atoms form an Fe_2O plane with the iron atoms (projection in the ab plane).

no nonmagnetic compounds isostructural with $Ba_2F_2Fe_2OSe_2$ were available, the phonon contribution was estimated by fitting the $C_p(T)$ curve to a polynomial function at temperatures far from the magnetic transition region (i.e., over the ranges 25–40 and 105–135 K). Conclusions drawn from the analysis of the temperature-dependence of the specific heat near the magnetic transition temperatures do not depend critically on the phonon background chosen.

Magnetic susceptibility measurements were performed using a Quantum Design MPMS SQUID magnetometer on powder samples of $Ba_2F_2Fe_2OSe_2$ (70.94 mg) and $Sr_2F_2Fe_2OS_2$ (138.0 mg) at 0.01 T over the temperature range 5–300 K. The raw data were corrected for the sample-holder contribution and core-electron diamagnetism.

Mössbauer studies were performed using a conventional spectrometer equipped with a $^{57}Co/Rh$ source (~ 10 mCi). The Mössbauer parameters were refined using standard least-squares procedures. The reference for the isomer shifts was metallic Fe at room temperature.

Neutron diffraction measurements were performed using the G4-1 2-axis diffractometer in the Orphee reactor at the Laboratoire Leon Brillouin (Saclay, France). Data were collected using a multidetector (800 cells, 0.1° apart) over a 2θ range of 10 – 90° . A monochromatized neutron beam ($\lambda = 2.427$ Å) was obtained using a focusing pyrolytic graphite (002) monochromator. A cylindrical vanadium sample holder with a diameter of 5 mm was filled with the powder sample and loaded in a cryofurnace ($T = 2$ – 450 K).

3. Synthesis and Structure Refinement

The four compounds $A_2F_2Fe_2OQ_2$ ($A = Sr, Ba$; $Q = S, Se$) built from the stacking of the known 2D SBUs $[A_2F_2]$ and $[Fe_2OQ_2]$, were expected to adopt a tetragonal structure of the $La_2O_2Fe_2OSe_2$ type (see Figure 2).²⁴ Analysis of the relevant interatomic distances suggests that the unit cell and the atomic parameters of $A_2F_2Fe_2OQ_2$ can be described by the space group $I4/mmm$. For the optimization of this “theoretical” structure on the basis of first-principles DFT calculations, the symmetry of the space group was lowered to $P4_2/mmc$, with the Fe and F

positions in two different crystallographic sites. This allowed us to take into consideration spin polarization and hence an antiferromagnetic (AFM) ordering of the spins of Fe^{2+} ions in which each iron atom is antiferromagnetically coupled with its neighboring Fe atoms within the Fe_2O planes (i.e., the ordered spin state AF1 discussed in Spin Exchange Interactions and Magnetic Structure, below). Table 1 presents the optimized predicted structure, which can serve as a model for comparison with experimental results.

We thus attempted to synthesize the predicted compounds by solid-state synthesis, as described in the Experimental Section. All of the syntheses performed at 800 °C resulted in dark homogeneous powders. The powders of $Ba_2F_2Fe_2OSe_2$ and $Sr_2F_2Fe_2OS_2$ melted in a congruent fusion process to form a mass of black crystals when a post-synthesis heat treatment was performed at 1000 °C. EDXS analyses of the crystal and powder samples of $A_2F_2Fe_2OQ_2$ confirmed the presence of the A, F, Fe, O, and Q elements. Moreover, the measured atomic ratios (see Table 2) were in good agreement with the theoretical values expected for the formulation $A_2F_2Fe_2OQ_2$ excluding O and F.

To confirm the structure prediction (see Table 1), X-ray diffraction data were recorded for a single crystal of $Ba_2F_2Fe_2OSe_2$. The cell parameters obtained correspond to a tetragonal cell with $a = 4.1946(6)$ Å and $c = 19.522(4)$ Å. The structural refinement was performed using the predicted structure but with the atomic positions in the space group $I4/mmm$. The refinement converged rapidly with a satisfying reliability factor (R_{obs}) of 0.0196 for the 243 observed reflections having $I > 2\sigma(I)$. The crystallographic data and refinement results are given in Table 3 and the atomic positions and isotropic displacement parameters in Table 4. The refinement confirmed that the experimental atomic and cell parameters of $Ba_2F_2Fe_2OSe_2$ are very close to the predicted values (compare Tables 4 and 1). A similar crystal structure refinement performed for a single crystal of

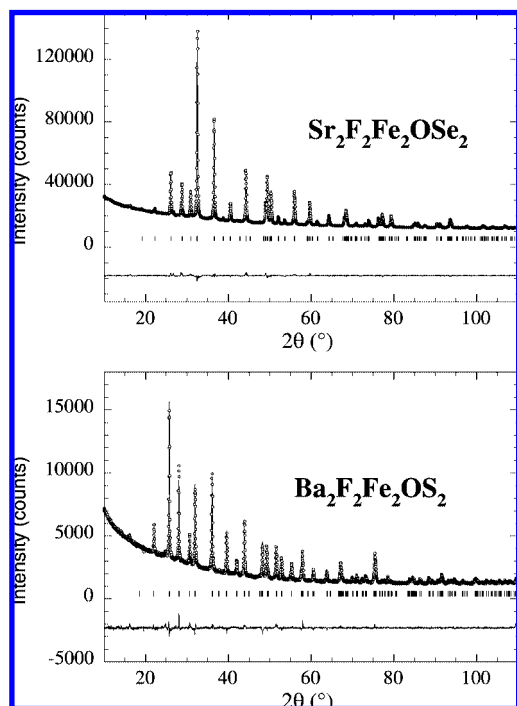


Figure 3. Observed X-ray diffraction patterns recorded for (top) $Sr_2F_2Fe_2OSe_2$ and (bottom) $Ba_2F_2Fe_2OS_2$. The black lines represent the intensities calculated using the Rietveld method. The bottom curves are the differences between the experimental and calculated intensities. The small marks indicate the Bragg peak positions of the target compounds. The small peak observed at 16.2° corresponds to a very small amount of an unidentified iron impurity.

Table 6. Selected Interatomic Distances and Bond Angles for $Ba_2F_2Fe_2OSe_2$, $Ba_2F_2Fe_2OS_2$, $Sr_2F_2Fe_2OSe_2$, and $Sr_2F_2Fe_2OS_2$

	A = Ba; Q = Se	A = Ba; Q = S	A = Sr; Q = Se	A = Sr; Q = S
Interatomic Distances (\AA) ^a				
d_{A-F} [4]	2.622(1)	2.613(1)	2.485(1)	2.470(1)
d_{A-O} [1]	3.308(1)	3.167(1)	3.235(1)	3.078(1)
d_{A-Q} [4]	3.348(1)	3.281(2)	3.229(1)	3.177(1)
d_{Fe-O} [2]	2.097(1)	2.062(1)	2.046(1)	2.020(1)
d_{Fe-Q} [4]	2.734(1)	2.649(2)	2.727(1)	2.633(1)
d_{Fe-Fe} [4]	2.966(1)	2.916(1)	2.894(1)	2.857(1)
Bond Angles (deg)				
Q-Fe-Q	79.80	77.76	82.76	79.78
	100.21	102.24	97.24	100.22
O-Fe-O	180	180	180	180
Q-Fe-O	90	90	90	90

^a Values in brackets give the number of equivalent distances of each type.

$Sr_2F_2Fe_2OS_2$ led to the same conclusion (see Tables 3 and 4). Likewise, Rietveld refinements of the X-ray powder patterns for $Ba_2F_2Fe_2OS_2$ and $Sr_2F_2Fe_2OSe_2$ samples (shown in Figure 3) readily converged to the predicted structures with satisfying reliability factors (see Tables 4 and 5).

Figure 2a shows the structure of $Ba_2F_2Fe_2OSe_2$, highlighting the stacking of the $[Ba_2F_2]$ and $[Fe_2OSe_2]$ 2D SBUs. Both the interatomic distances within the mixed O/Se distorted octahedral environment of the Fe atoms (see Table 6 and Figure 2b–d) and the results of bond valence sum calculations are in agreement with the +2 oxidation state for the iron atoms (1.92 and 2.04 for $Ba_2F_2Fe_2OSe_2$ and $Sr_2F_2Fe_2OS_2$, respectively). Within the Fe_2OQ_2 layer (Figure 2e), the nearest-neighbor $Fe\cdots Fe$ distance ranges from 2.966 \AA in $Ba_2F_2Fe_2OSe_2$ to 2.857 \AA in $Sr_2F_2Fe_2OS_2$.

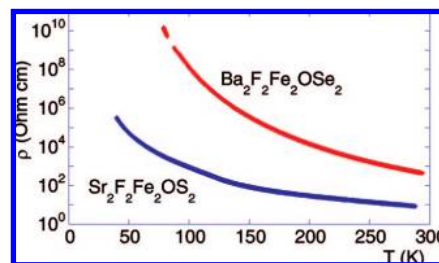


Figure 4. Resistivity as a function of temperature for (blue) $Sr_2F_2Fe_2OS_2$ and (red) $Ba_2F_2Fe_2OSe_2$.

4. Electrical Resistivity

Figure 4 shows the temperature dependence of the electrical resistivity measured for single-crystal samples of $Ba_2F_2Fe_2OSe_2$ and $Sr_2F_2Fe_2OS_2$. Both compounds are non-metallic, and their electrical resistivities exhibit an activated behavior, $\rho(T) = \rho_0 \exp(E_a/k_B T)$, where k_B is Boltzmann's constant. The activation energies (E_a) were 0.28 and 0.10 eV for $Ba_2F_2Fe_2OSe_2$ and $Sr_2F_2Fe_2OS_2$, respectively. The room-temperature resistivity of $Sr_2F_2Fe_2OS_2$ is 2 orders of magnitude smaller than that of $Ba_2F_2Fe_2OSe_2$. To account for this observation, it should be recalled that the nearest-neighbor $Fe\cdots Fe$, $Fe-Q$, and $Fe-O$ distances are shorter in $Sr_2F_2Fe_2OS_2$ than in $Ba_2F_2Fe_2OSe_2$ (see Table 6). For nonmagnetic semiconductors, replacing Se atoms with more-electronegative S atoms increases the band gap, and this feature is widely used to tune the band gaps of semiconductors such as $CuIn_{1-x}Ga_xS_{2-y}Se_y$ (CIGS) used for solar cells. To a lesser extent, replacing Sr atoms with more-electropositive Ba atoms also increases the band gap. For example, for $A_2F_2SnQ_3$ ($A = Sr, Ba; Q = S, Se$), the optical band gap increases from 2.24 and 2.49 eV for $Sr_2F_2SnSe_3$ and $Ba_2F_2SnSe_3$, respectively, to 3.06 eV and 3.21 eV for $Sr_2F_2SnS_3$ and $Ba_2F_2SnS_3$, respectively.¹⁷ The activated electrical conductivities with small activation energies for $Ba_2F_2Fe_2OSe_2$ and $Sr_2F_2Fe_2OS_2$ cannot be explained from the viewpoint of an energy gap between the valence and conduction bands of a nonmagnetic insulator. As will be shown in the next section, these oxyfluorides are magnetic semiconductors (i.e., Mott insulators) with unpaired spins at the Fe^{2+} sites. For a magnetic semiconductor, electrical conduction results from electron-hopping between adjacent spin sites. Thus, because of its shorter $Fe\cdots Fe$, $Fe-Q$, and $Fe-O$ distances, $Sr_2F_2Fe_2OS_2$ has a greater integral for hopping between adjacent Fe^{2+} sites and hence a larger electrical conductivity than does $Ba_2F_2Fe_2OSe_2$. The compound $LaOFeP$, which has a square planar lattice of Fe atoms (see Table 7), is metallic and was recently found to be superconducting.³³ The nearest-neighbor $Fe\cdots Fe$ distance in $LaOFeP$ is 2.803 \AA , which is only 0.054 \AA shorter than that in $Sr_2F_2Fe_2OS_2$. Therefore, it would be of interest to examine whether $Sr_2F_2Fe_2OS_2$ might undergo an insulator-to-metal transition upon application of external pressure. Conversely, attempts to electronically dope $A_2F_2Fe_2OQ_2$ by substituting a small amount (<10 %) of Sr or Ba with Na in order to induce an insulator-to-metal transition were not successful but led to a new mixed-valence compound, $Ba_2F_2Fe_{1.5}S_3$.³⁴

5. Magnetic Properties

The temperature dependence of the magnetic susceptibilities of $Ba_2F_2Fe_2OSe_2$ ($d_{Fe-Fe} = 2.966 \text{\AA}$) and $Sr_2F_2Fe_2OS_2$ (d_{Fe-Fe}

Table 7. Evolution of Magnetic and Electrical Properties with Decreasing Cell Parameter a and Fe–O and Fe–Fe distances for the series of compounds $\text{Ba}_2\text{F}_2\text{Fe}_2\text{OSe}_2$, $\text{Ba}_2\text{F}_2\text{Fe}_2\text{OS}_2$, $\text{Sr}_2\text{F}_2\text{Fe}_2\text{OSe}_2$, $\text{Sr}_2\text{F}_2\text{Fe}_2\text{OS}_2$, and LaOFeP^a

	$\text{Ba}_2\text{F}_2\text{Fe}_2\text{OSe}_2$	$\text{Ba}_2\text{F}_2\text{Fe}_2\text{OS}_2$	$\text{Sr}_2\text{F}_2\text{Fe}_2\text{OSe}_2$	$\text{Sr}_2\text{F}_2\text{Fe}_2\text{OS}_2$	LaOFeP
a (Å)	4.1946(6)	4.1238(2)	4.0925(2)	4.0400(6)	3.964(1)
$d_{\text{Fe–O}}$ (Å)	2.097(1)	2.062(1)	2.046(1)	2.020(1)	–
$d_{\text{Fe–Fe}}$ (Å)	2.966	2.916	2.894	2.857	2.803
susceptibility	AFM	AFM	AFM	AFM	Pauli
T_N (K)	83.6	94–95	95–97	106.2	–
resistivity	semiconducting	semiconducting	semiconducting	semiconducting	metallic
E_g (eV)	0.28	–	–	0.10	–

^aThe comparison with LaOFeP shows that the $\text{A}_2\text{F}_2\text{Fe}_2\text{OQ}_2$ compounds are close to the insulator-to-metal transition and could exhibit superconductivity upon application of external pressure.

= 2.857 Å) is shown in Figure 5a. The susceptibility shows a broad maximum at high temperature, indicating the presence of dominant AFM interactions. Moreover, the susceptibility-versus-temperature curves show anomalies at ~85 and ~105 K for $\text{Ba}_2\text{F}_2\text{Fe}_2\text{OSe}_2$ and $\text{Sr}_2\text{F}_2\text{Fe}_2\text{OS}_2$, respectively. ($\text{Sr}_2\text{F}_2\text{Fe}_2\text{OSe}_2$ and $\text{Ba}_2\text{F}_2\text{Fe}_2\text{OS}_2$ exhibit similar susceptibility curves, with anomalies at ~96 and ~94 K, respectively). The specific heat of $\text{Ba}_2\text{F}_2\text{Fe}_2\text{OSe}_2$ (Figure 5b) exhibits a peak at 83.6 K, which is close to the temperature at which the magnetic susceptibility anomaly occurs. Thus, the magnetic and calorimetric anomalies suggest the existence of a long-range-order AFM transition in this compound at an AFM ordering temperature (Néel temperature) of $T_N \approx 85$ K. This is further confirmed by neutron diffraction data collected for $\text{Ba}_2\text{F}_2\text{Fe}_2\text{OSe}_2$ (see Figure 5d,e), which show magnetic peaks below 83.6 K (see below for further discussion). At high temperature, the neutron powder patterns were fully indexed with a tetragonal cell, while at low temperature, the neutron powder patterns revealed an incommensurate magnetic phase. For example, for the powder pattern recorded at 1.5 K, the nuclear structure was refined with a tetragonal cell [$a = 4.222(2)$ Å, $c = 19.323(7)$ Å], and the new magnetic peaks could be indexed in a supercell [$a = b = 5.970(3)$ Å, $c = 19.323(7)$ Å] with a modulation vector $\mathbf{q} = (0.41727, 0.00000, 0.00000)$. These results together with the observation of activated electrical conductivities show that $\text{Sr}_2\text{F}_2\text{Fe}_2\text{OS}_2$ and $\text{Ba}_2\text{F}_2\text{Fe}_2\text{OSe}_2$ are magnetic semiconductors. This conclusion is also consistent with the results of our ^{57}Fe Mössbauer measurements on $\text{Ba}_2\text{F}_2\text{Fe}_2\text{OSe}_2$ and $\text{Sr}_2\text{F}_2\text{Fe}_2\text{OS}_2$ (Figures 6a and 7a). From high temperatures down to T_N , the Mössbauer spectra of $\text{Ba}_2\text{F}_2\text{Fe}_2\text{OSe}_2$ and $\text{Sr}_2\text{F}_2\text{Fe}_2\text{OS}_2$ are composed of a doublet. The refined parameters for the spectra of $\text{Ba}_2\text{F}_2\text{Fe}_2\text{OSe}_2$ and $\text{Sr}_2\text{F}_2\text{Fe}_2\text{OS}_2$, respectively, at 300 K had the following values: isomer shifts (δ) of 0.92 and 0.90 mm/s; quadrupole splittings (Δ) of 2.21 and 1.91 mm/s. These isomer shift values exclude the presence of Fe^{3+} ions. Conversely, they lie between the corresponding values found for pure chalcogenides (0.8–0.9 mm/s)^{35,36} and oxides (1.03–1.28 mm/s)^{37,38} containing high-spin Fe^{2+} ions. Magnetic spectra were found at temperatures below T_N , which supports the presence of high-spin Fe^{2+} ions. For all of the spectra recorded for $T < T_N$, we extracted the hyperfine magnetic field value (H) in order to determine the evolution of H/H_{sat} with respect to T/T_N (Figures

6b and 7b), where the H_{sat} values near 4 K for $\text{Ba}_2\text{F}_2\text{Fe}_2\text{OSe}_2$ and $\text{Sr}_2\text{F}_2\text{Fe}_2\text{OS}_2$ are 204 and 206.5 kG, respectively. The slopes (β) of the $\log(H/H_{\text{sat}})$ -versus- $\log(1 - T/T_N)$ plot (see the insets in Figures 6b and 7b) were 0.118 for $\text{Ba}_2\text{F}_2\text{Fe}_2\text{OSe}_2$ and 0.15 for $\text{Sr}_2\text{F}_2\text{Fe}_2\text{OS}_2$. These β values are close to the theoretical value of 0.125 expected for a 2D Ising system.³⁹

The inset of Figure 5b shows the magnetic contribution to the specific heat of $\text{Ba}_2\text{F}_2\text{Fe}_2\text{OSe}_2$ after subtraction of the phonon contribution, which is preponderant at temperatures higher than 10 K. This magnetic contribution to the specific heat was plotted as a function of $\log(1 - T_N/T)$ in Figure 5c, which shows two straight lines corresponding to the $T > T_N$ and $T < T_N$ regions. In addition, the magnetic specific heats above and below T_N are similar. This is consistent with the conclusion that the magnetic transitions of $\text{Ba}_2\text{F}_2\text{Fe}_2\text{OSe}_2$ and $\text{Sr}_2\text{F}_2\text{Fe}_2\text{OS}_2$ belong to the 2D Ising system universality class.

Figure 5d shows the temperature dependence of the most intense magnetic peak ($2\theta = 38^\circ$) in our neutron powder diffraction data for $\text{Ba}_2\text{F}_2\text{Fe}_2\text{OSe}_2$. The magnetic moment on Fe, M_{Fe} , is proportional to the square root of the normalized integrated magnetic peak intensity. The temperature dependence of M_{Fe} can be fitted to the power law $M_{\text{Fe}}(T) = C(1 - T/T_N)^\beta$ with $\beta = 0.15$. This β value is consistent with the corresponding one obtained from the Mössbauer measurements ($\beta = 0.118$).

All of the measurements described above clearly support the conclusion that the compounds $\text{A}_2\text{F}_2\text{Fe}_2\text{OQ}_2$ ($\text{A} = \text{Sr}, \text{Ba}; \text{Q} = \text{S}, \text{Se}$) with Fe^{2+} ions at octahedral sites exhibit an AFM transition belonging to the 2D Ising universality class. At this point, we note (a) that 2D Ising systems are the only low-dimensional compounds for which a transition to a long-range-ordered state is theoretically expected^{39,40} and (b) that some other magnetic systems containing Fe^{2+} ions exhibit Ising-like behavior with an AFM transition.³⁵ However, we also note that the Ising behavior observed in the $\text{A}_2\text{F}_2\text{Fe}_2\text{OQ}_2$ compounds is quite puzzling, because the iron atoms are located at octahedral sites. Uniaxial magnetic properties are not expected for Fe^{2+} ions at perfectly octahedral sites (O_h symmetry),⁴¹ although such ions can produce substantially anisotropic magnetic properties. Even though the site symmetry does not allow $\text{A}_2\text{F}_2\text{Fe}_2\text{OQ}_2$ to be a pure Ising system, the distorted octahedral sites of the Fe^{2+} ions in these compounds (D_{2h} symmetry) allow for strong anisotropic magnetic properties, leading to Ising-like behavior.

In the series of compounds $\text{A}_2\text{F}_2\text{Fe}_2\text{OQ}_2$ ($\text{A} = \text{Sr}, \text{Ba}; \text{Q} = \text{S}, \text{Se}$), substitution of the alkaline-earth and/or chalcogen atoms affects the distortion of the Fe^{2+} octahedral sites, as evidenced by the increase of the Q–Fe–Q angle upon replacement of S by Se or Ba by Sr (see Table 6). Moreover, all of the distances, including the Fe···Fe, Fe–O, and Fe–Q distances in the $[\text{Fe}_2\text{OQ}_2]$ layers, are systematically increased

(33) Kamihara, Y.; Hiramatsu, H.; Hirano, H.; Kawamura, R.; Yanagi, H.; Kamiya, T.; Hosono, H. *J. Am. Chem. Soc.* **2006**, *128*, 10012.

(34) Kabbour, H.; Cario, L. *Inorg. Chem.* **2008**, *47*, 1648.

(35) Joy, P. A.; Vasudevan, S. *Chem. Mater.* **1993**, *5*, 1182.

(36) Morimoto, S.; Matsushita, Y.; Ueda, Y.; Kawase, M.; Saito, T.; Nakamura, S.; Nasu, S. *J. Magn. Magn. Mater.* **2007**, *310*, E962.

(37) Menil, F. *J. Phys. Chem. Solids* **1985**, *46*, 763–789.

(38) Benmokhtar, S.; El Jazouli, A.; Aatiq, A.; Chaminade, J. P.; Gravereau, P.; Wattiaux, A.; Fournes, L.; Grenier, J. C. *J. Solid State Chem.* **2007**, *180*, 2004.

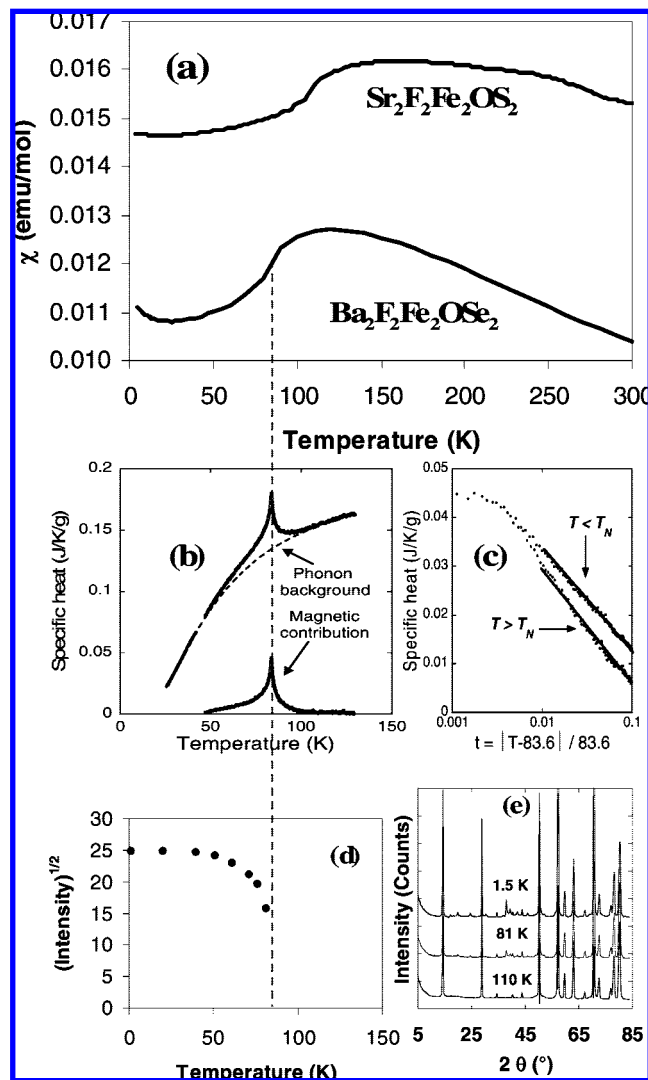


Figure 5. Characterization of the magnetic transition for $Ba_2F_2Fe_2OSe_2$ and $Sr_2F_2Fe_2OS_2$: (a) Temperature dependence of the magnetic susceptibility. (b) Evolution of the specific heat of $Ba_2F_2Fe_2OSe_2$ with temperature; the inset highlights the magnetic contribution. The dotted line corresponds to the estimated phononic contribution, which was used to extract the magnetic contribution. (c) Evolution of the magnetic specific heat of $Ba_2F_2Fe_2OSe_2$ with the logarithm of $t \equiv |T - T_N|/T_N$. The straight lines observed for $0.01 < t < 0.1$ indicate that the specific heat follows a logarithmic divergence close to T_N . The amplitude ratio $A+/A-$, corresponding to the slope ratio in this representation, is very close to 1. Both features are expected on the basis of the 2D Ising model. (d) Evolution of the neutron diffraction intensity of the most intense magnetic peak for $Ba_2F_2Fe_2OSe_2$ ($2\theta = 38^\circ$) as a function of temperature. The power-law fit of this curve gives a critical exponent of 0.15, indicating a 2D Ising model. (e) Neutron diffraction patterns of $Ba_2F_2Fe_2OSe_2$ collected before and after the AFM transition.

upon replacement of S by Se or Sr by Ba (see Table 6). As shown in Table 7, T_N increases from 83.6 K in $Ba_2F_2Fe_2OSe_2$ to 106.2 K in $Sr_2F_2Fe_2OS_2$. This suggests that isovalent chemical substitutions in the $A_2F_2Fe_2OQ_2$ family induce a chemical pressure effect that enhances the spin exchange interactions. A similar observation has been made for the oxysulfide compound $Sr_2Cu_2CoO_2S_2$ containing CoO_2 square planar layers.⁴²

6. Spin Exchange Interactions and Magnetic Structure

In this section, we discuss our investigation of the magnetic properties of $Ba_2F_2Fe_2OSe_2$ and $Sr_2F_2Fe_2OS_2$ using first-

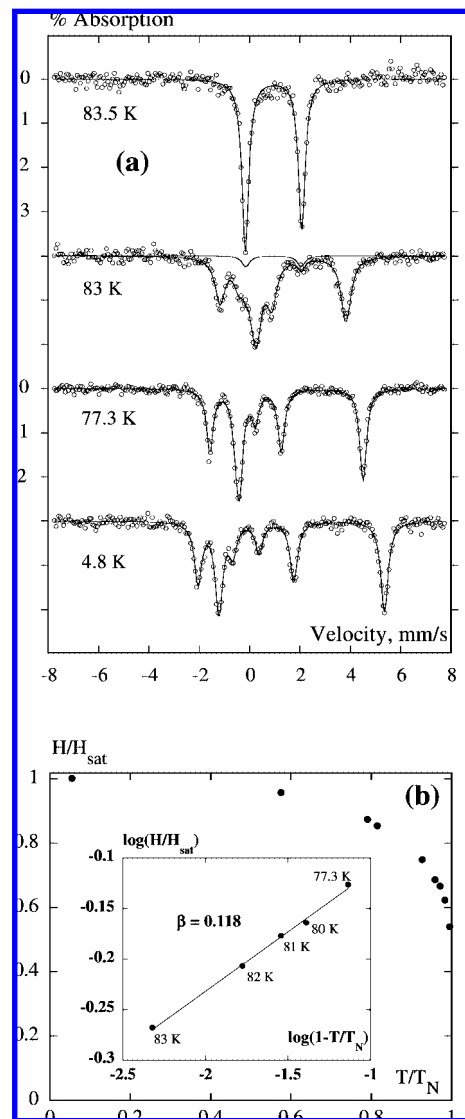


Figure 6. (a) Mössbauer spectra of $Ba_2F_2Fe_2OSe_2$ collected before and after the AFM transition. (b) Plots of H/H_{sat} vs T/T_N and (inset) $\log(H/H_{sat})$ vs $\log(1 - T/T_N)$ lead to a value of 0.118 for the critical exponent (β), indicating 2D Ising magnetic interactions. A weak nonmagnetic contribution appears in the magnetic spectrum recorded at 83 K. Conversely, in the nonmagnetic spectrum recorded at 83.5 K, the doublet asymmetry and some absorption between the two lines could be due to a very weak magnetic contribution (which could not be significantly refined). In view of the drastic increase of the hyperfine field just below T_N (see inset), which is characteristic of 2D magnetic behavior, defects or very small changes in stoichiometry could easily explain the presence of domains with slightly different magnetic-ordering temperatures.

principles DFT electronic structure calculations. To properly describe the strong electron correlation associated with the 3d electrons of Fe, the GGA plus on-site repulsion (U) method (GGA+ U) was employed.⁴³ As depicted in Figure 8, there are three intralayer spin exchange interactions that must be considered for $Ba_2F_2Fe_2OSe_2$ and $Sr_2F_2Fe_2OS_2$: J_1 , J_2 , and J_3 are the exchange parameters correspond to spin exchange through corner-sharing Fe–O–Fe, edge-sharing Fe–Q–Fe, and face-sharing Fe–O–Fe/Fe–Q–Fe linkages, respectively. These exchange parameters can be determined by calculating the total energies of several ordered spin states and then equating differences in these energies to the corresponding energy differences expected on the basis of the spin Hamiltonian expressed in terms of J_1 , J_2 , and J_3 .^{44–46} Since there are three

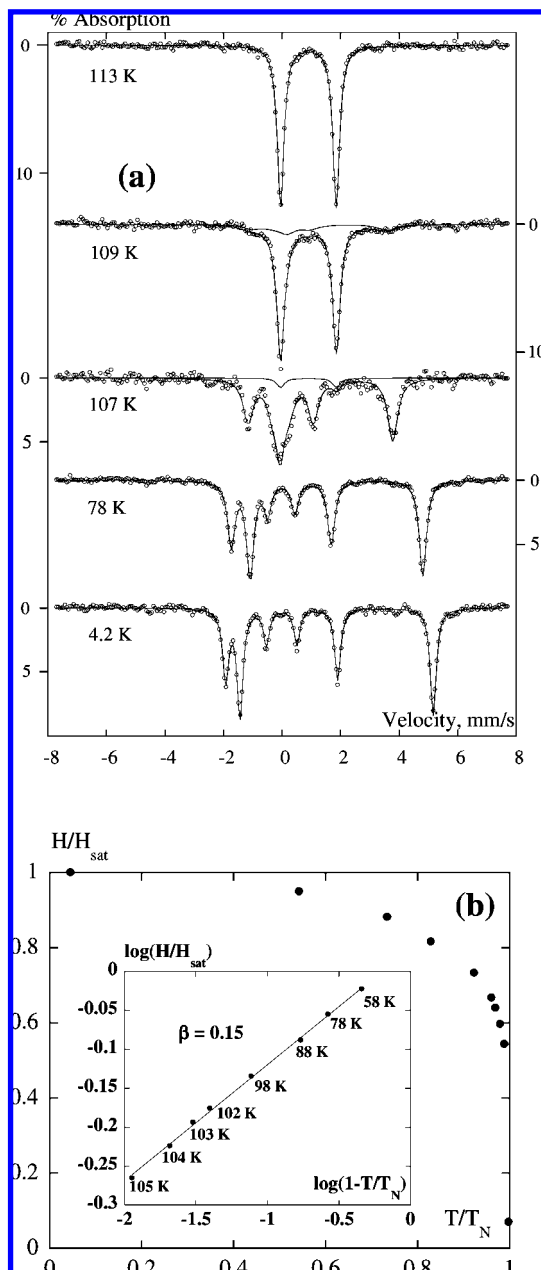


Figure 7. (a) Mössbauer spectra of $\text{Sr}_2\text{F}_2\text{Fe}_2\text{OS}_2$ collected before and after the AFM transition. (b) Plots of H/H_{sat} vs T/T_N and (inset) $\log(H/H_{\text{sat}})$ vs $(1 - T/T_N)$ lead to a value of 0.15 for the critical exponent (β), indicating 2D Ising magnetic interactions. Analogous to what was observed for $\text{Ba}_2\text{F}_2\text{Fe}_2\text{OSe}_2$ (Figure 6), a weak magnetic contribution is present at 109 K and a weak nonmagnetic contribution at 107 K.

parameters to determine, we considered the four ordered spin states FM, AF1, AF2, and AF3 depicted in Figure 9. The choice of broken-symmetry states such as AF2 and AF3 may seem strange, but such states facilitate extraction of the spin exchange parameters (see below). The relative total energies per chemical unit cell (i.e., per two formula units) obtained for the FM, AF1, AF2, and AF3 states of $\text{Ba}_2\text{F}_2\text{Fe}_2\text{OSe}_2$ and $\text{Sr}_2\text{F}_2\text{Fe}_2\text{OS}_2$ by performing GGA+ U calculations with several different U values are summarized in Table 8. It should be pointed out that spin-polarized GGA calculations (i.e., GGA+ U calculations with $U = 0$) lead to metallic states for $\text{Ba}_2\text{F}_2\text{Fe}_2\text{OSe}_2$ and $\text{Sr}_2\text{F}_2\text{Fe}_2\text{OS}_2$. Given that these compounds are magnetic insulators, GGA+ U calculations with nonzero U are necessary to properly describe their magnetic properties. For both compounds, the total energies

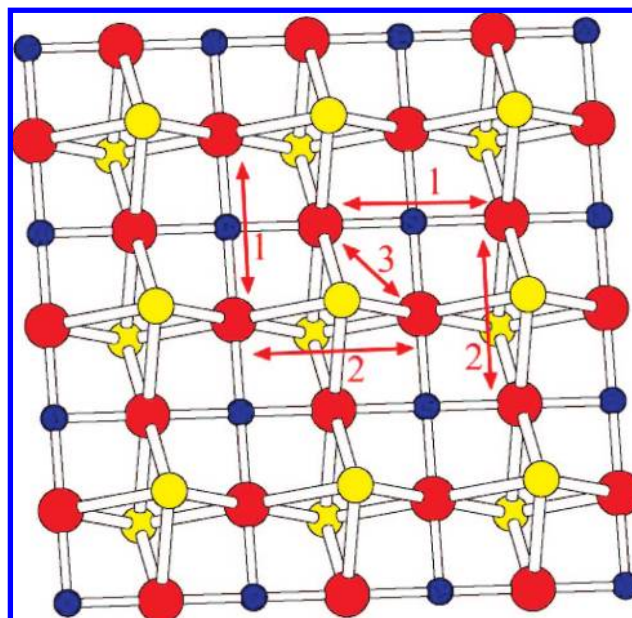


Figure 8. Spin exchange paths J_1 , J_2 , and J_3 present in each Fe_2OQ_2 layer of $\text{A}_2\text{F}_2\text{Fe}_2\text{OQ}_2$. The Fe, Q, and O atoms are represented by red, yellow, and blue circles, respectively. The labels 1, 2 and 3 represent J_1 , J_2 , and J_3 , respectively.

of the four ordered spin states increased in the order AF1 < AF3 < AF2 < FM.

To extract the values of the spin exchange parameters J_1 – J_3 from the above electronic structure calculations, we expressed the total spin exchange interaction energies of the four ordered spin states in terms of the Ising spin Hamiltonian

$$\hat{H} = - \sum_{i < j} J_{ij} \hat{S}_{iz} \hat{S}_{jz} \quad (1)$$

where J_{ij} ($=J_1$, J_2 , or J_3) is the spin exchange parameter for the spin exchange interaction between spin sites i and j and \hat{S}_{iz} and \hat{S}_{jz} are the operators for the z components of the spin angular momentum at spin sites i and j , respectively. Next, by applying the energy expressions obtained for spin dimers with N unpaired spins per spin site (in the present case, $N = 4$ for the high-spin Fe^{2+} ions),^{47,48} we derived the following formulas for the total spin exchange energies per chemical unit cell for the four ordered spin states:

$$E_{\text{FM}} = (-8J_3 - 4J_2 - 4J_1)N^2/4 \quad (2a)$$

$$E_{\text{AF1}} = (8J_3 - 4J_2 - 4J_1)N^2/4 \quad (2b)$$

$$E_{\text{AF2}} = (-4J_3 - 2J_2 - 4J_1)N^2/4 \quad (2c)$$

$$E_{\text{AF3}} = (-4J_3 - 2J_2 - 2J_1)N^2/4 \quad (2d)$$

By equating the energy differences between pairs of states written in terms of J_1 , J_2 , and J_3 to the corresponding electronic energy differences obtained from the DFT calculations, we obtained the values of J_1 , J_2 , and J_3 summarized in Table 9.

For both $\text{Ba}_2\text{F}_2\text{Fe}_2\text{OSe}_2$ and $\text{Sr}_2\text{F}_2\text{Fe}_2\text{OS}_2$, our GGA+ U calculations showed that the Fe–O–Fe spin exchange J_1 and the Fe–O–Fe/Fe–Q–Fe spin exchange J_3 are AFM, while the Fe–Q–Fe spin exchange J_2 is ferromagnetic (FM). The main antiferromagnetic interaction between the iron spins is mediated through the Fe–O–Fe 180° superexchange within the $[\text{Fe}_2\text{O}]$ planes, which is in accord with the Goodenough–Kanamori

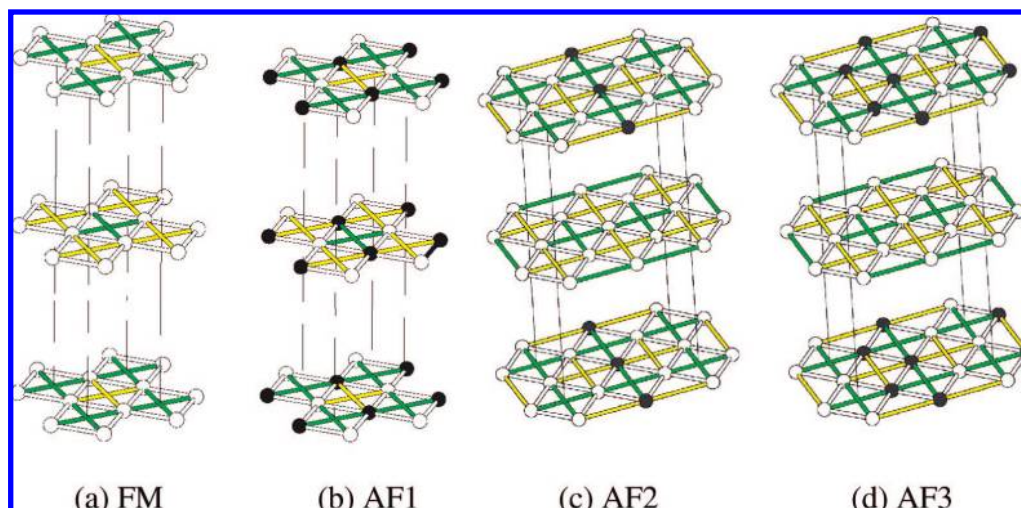


Figure 9. Schematic representations of the four ordered spin states FM, AF1, AF2, and AF3 of $A_2F_2Fe_2OQ_2$ that were employed in order to extract the spin exchange parameters J_1 , J_2 , and J_3 . For simplicity, only the Fe atoms are shown, and the spin-up and spin-down Fe sites are represented by empty and filled circles, respectively. The green, yellow, and white cylinders represent the J_1 , J_2 , and J_3 spin exchange paths, respectively.

Table 8. Relative Energies ΔE (meV/unit cell) of the FM, AF1, AF2, and AF3 States of $Ba_2Se_2Fe_2OF_2$ and $Sr_2S_2Fe_2OF_2$ Obtained from GGA+ U Calculations

U (eV)	FM	AF1	AF2	AF3
		(a) $Ba_2Se_2Fe_2OF_2$		
1.5	0	-156	-19.7	-79.8
3.0	0	-164	-22.6	-61.7
4.5	0	-145	-19.5	-47.3
		(b) $Sr_2S_2Fe_2OF_2$		
1.5	0	-158	-36.3	-83.4
3.0	0	-160	-31.3	-63.7
4.5	0	-145	-29.3	-51.8

Table 9. Values of the Spin Exchange Parameters J_1 , J_2 , and J_3 (meV) for $Ba_2Se_2Fe_2OF_2$ and $Sr_2S_2Fe_2OF_2$ Estimated from the GGA+ U Calculations

U (eV)	J_1	J_2	J_3
	(a) $Ba_2Se_2Fe_2OF_2$		
1.5	-7.5	2.4	-2.4
3.0	-4.9	2.3	-2.6
4.5	-3.5	2.1	-2.3
	(b) $Sr_2S_2Fe_2OF_2$		
1.5	-5.9	0.4	-2.5
3.0	-4.1	1.1	-2.5
4.5	-2.8	0.9	-2.3

rules. A given Fe^{2+} site has four J_3 interactions, two J_2 interactions, and two J_1 interactions with surrounding Fe^{2+} ions. It is therefore clear that the overall spin exchange interaction between nearest-neighbor spins is AFM, which is in agreement with the experimental observations. These calculations are also consistent with the experimental susceptibilities measured for $A_2F_2Fe_2OQ_2$ compounds with high-spin Fe^{2+} ($S = 2$) ions.

In each layer of Fe^{2+} ions parallel to the ab plane, the Fe^{2+} ions form a checkerboard pattern (Figure 10a). Table 9 shows that $|J_1| > |J_3| \geq J_2$ for small U and that $|J_1|$ becomes smaller but remains slightly greater than $|J_3|$ for large U . In the limit where $|J_1| \gg |J_3| \geq J_2$, the strongest spin exchange, J_1 , forms one set of uniform 1D AFM chains along the a direction and another set of uniform 1D AFM chains along the b direction (Figure 10b,c). In each set, an FM interchain coupling leads to the “1A2F” spin arrangement (Figure 10b) and an AFM interchain coupling to the “1A2A” spin arrangement (Figure

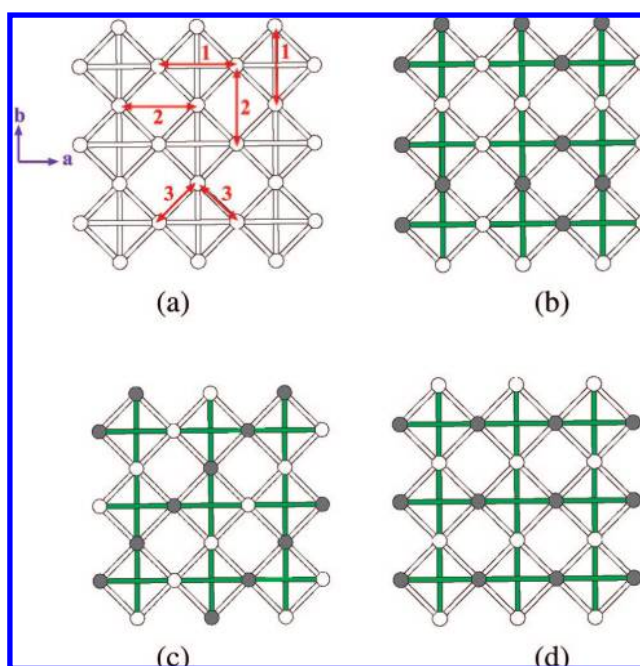


Figure 10. (a) Checkerboard pattern of high-spin Fe^{2+} ions in each Fe_2OQ_2 layer of $A_2F_2Fe_2OQ_2$ parallel to the ab plane. Each circle represents an Fe^{2+} ion, and the labels 1, 2, and 3 refer to the spin exchange interactions J_1 , J_2 , and J_3 , respectively. (b) The 1A2F spin arrangement, in which all of the J_1 and J_2 paths have AFM and FM couplings, respectively. (c) The 1A2A spin arrangement, in which all of the J_1 and J_2 paths have AFM coupling. (d) The 2F3A spin arrangement, in which all of the J_2 and J_3 paths have FM and AFM couplings, respectively. In (b–d), the spin-up and spin-down sites are indicated by empty and filled circles, respectively.

10c). In both the 1A2F and 1A2A spin arrangements, half of the J_3 interactions are frustrated, so their contributions to the stability of the spin arrangements are zero. Since the J_2 interactions are FM, the 1A2F spin arrangement is more stable than the 1A2A spin arrangement. In the “2F3A” spin arrangement shown in Figure 10d, all of the J_1 interactions become frustrated as a consequence of the AFM coupling for all of the J_3 paths and the FM coupling for all of the J_2 paths. The 1A2F spin arrangement should be more stable than the 2F3A spin

arrangement when $|J_1| > 2|J_3|$, but the opposite should be true when $|J_1| < 2|J_3|$.

For the most realistic values of U (3 and 4.5 eV), our calculations showed that $|J_1| < 2|J_3|$, with $|J_1|/2|J_3|$ ranging from 0.6 to 0.94. In the limit where $|J_1| \gg 2|J_3|$, the spin exchange interactions of the 2D checkerboard lattice may be approximated by Ising and Heisenberg 2D square lattice models with ions of spin $S = 2$ and nearest-neighbor AFM spin exchange J_3 . In this case, these models give the following formulas showing how the temperature T_{\max} at which the magnetic susceptibility reaches a maximum is related to $|J_3|$:⁴⁹

$$\text{Ising 2D square lattice: } \frac{k_B T_{\max}}{|J_3|} \approx 13.9 \quad (3a)$$

$$\text{Heisenberg 2D square lattice: } \frac{k_B T_{\max}}{|J_3|} \approx 24.8 \quad (3b)$$

For $\text{Ba}_2\text{F}_2\text{Fe}_2\text{OSe}_2$ and $\text{Sr}_2\text{F}_2\text{Fe}_2\text{OS}_2$, T_{\max} is in the 120–150 K range, so $|J_3|$ is estimated to be 0.7–0.9 meV for the Ising square lattice and 0.4–0.5 meV for the Heisenberg square lattice. These values are considerably smaller than the calculated $|J_3|$ values. This result shows that both of the AFM interactions J_1 and J_3 must be considered in order to properly describe the magnetic properties of the $\text{A}_2\text{F}_2\text{Fe}_2\text{OQ}_2$ compounds. This is not surprising, as J_1 and J_3 were calculated to be of the same magnitude, i.e., the system is far from the $|J_1| \gg 2|J_3|$ limit. As mentioned above, J_1 and J_3 interactions therefore form a frustrated AFM checkerboard lattice (see Figure 10d) that is not critically modified by the FM interaction J_2 that couples spins along the diagonals of “empty” squares of the lattice (see Figure 10). Frustrated AFM checkerboard lattices have received much attention in the last decade as a prototype frustrated low-dimensional system in which long-range order is in competition

with a disordered state related to geometric spin frustration.⁵⁰ Despite the frustration, an ordered Néel state may arise in the checkerboard lattice for spin values larger than $S = 1/2$ in the isotropic case (here this applies when $J_1 = J_3 = J$).⁵⁰ Furthermore, theoretical calculations for the isotropic ($J_1 = J_3 = J$) Ising checkerboard predict that the Néel temperature is given by $T_N = 3.73|J|/k_B$.⁵¹ For $|J| = 2.55$ meV ($\approx |J_3|$ for $\text{Sr}_2\text{F}_2\text{Fe}_2\text{OS}_2$ from Table 9b), the Néel temperature of 110 K calculated using this formula compares very well with the experimental T_N value of 106.2 K (see Table 7). This good agreement between theory and experiment indicates that the checkerboard lattice is appropriate for describing the magnetic properties of $\text{A}_2\text{F}_2\text{Fe}_2\text{OQ}_2$. Checkerboard spin lattices are scarce. In that respect, the first experimental realization of a frustrated $S = 2$ AFM checkerboard spin lattice in the $\text{A}_2\text{F}_2\text{Fe}_2\text{OQ}_2$ compounds is of special interest.

7. Concluding Remarks

We have synthesized a novel family of compounds, $\text{A}_2\text{F}_2\text{Fe}_2\text{OQ}_2$ ($A = \text{Sr, Ba}$; $Q = \text{S, Se}$), that have Fe_2O square planar layers with an anti- CuO_2 -type structure. Our resistivity, magnetic susceptibility, and specific heat measurements showed that the $\text{A}_2\text{F}_2\text{Fe}_2\text{OQ}_2$ compounds are magnetic semiconductors and undergo an AFM transition below 83.6–106.2 K. The temperature dependence of the magnetic properties of $\text{Ba}_2\text{F}_2\text{Fe}_2\text{OSe}_2$ and $\text{Sr}_2\text{F}_2\text{Fe}_2\text{OS}_2$ is reasonably well described by an Ising 2D square net model. The spin exchange interactions in $\text{Ba}_2\text{F}_2\text{Fe}_2\text{OSe}_2$ and $\text{Sr}_2\text{F}_2\text{Fe}_2\text{OS}_2$ estimated from first-principles DFT calculations showed that the corner-sharing Fe–O–Fe and face-sharing Fe–O–Fe/Fe–Q–Fe spin exchange interactions (J_1 and J_3 , respectively) are both AFM and form a checkerboard spin lattice. The $\text{A}_2\text{F}_2\text{Fe}_2\text{OQ}_2$ ($A = \text{Sr, Ba}$; $Q = \text{S, Se}$) compounds represent the first experimental realization of an $S = 2$ antiferromagnetic checkerboard spin lattice.

Acknowledgment. André Gilles (CEA-LLB, France) is thanked for his help in performing the powder neutron diffraction experiments. The work at North Carolina State University was supported by the Office of Basic Energy Sciences, Division of Materials Sciences, U.S. Department of Energy, under Grant DE-FG02-86ER45259.

Supporting Information Available: Crystallographic information files (CIF) for the compounds $\text{A}_2\text{F}_2\text{Fe}_2\text{OQ}_2$ ($A = \text{Sr, Ba}$; $Q = \text{S, Se}$). This material is available free of charge via the Internet at <http://pubs.acs.org>.

JA711139G

- (39) Onsager, L. *Phys. Rev. B* **1944**, *65*, 117.
 (40) de Jongh, L. J. In *Magnetic Properties of Layered Transition Metal Compounds*; de Jongh, L. J., Ed.; Kluwer Academic Publishers: Dordrecht, The Netherlands, 1990; pp 1–47.
 (41) Dai, D.; Whangbo, M.-H. *Inorg. Chem.* **2005**, *44*, 4407.
 (42) Okada, S.; Matoba, M.; Yoshida, H.; Ohoyama, K.; Yamaguchi, Y. *J. Phys. Chem. Solids* **2002**, *63*, 983.
 (43) Dudarev, S. L.; Botton, G. A.; Savrasov, S. Y.; Humphreys, C. J.; Sutton, A. P. *Phys. Rev. B* **1998**, *57*, 1505.
 (44) Whangbo, M.-H.; Koo, H.-J.; Dai, D. *J. Solid State Chem.* **2003**, *176*, 417.
 (45) Dai, D.; Whangbo, M.-H.; Koo, H.-J.; Rocquefelte, X.; Jobic, S.; Villesuzanne, A. *Inorg. Chem.* **2005**, *44*, 2407.
 (46) Chartier, A.; D’Arco, P.; Dovesi, R.; Saunders, V. R. *Phys. Rev. B* **1991**, *60*, 14042.
 (47) Dai, D.; Whangbo, M.-H. *J. Chem. Phys.* **2001**, *114*, 2887.
 (48) Dai, D.; Whangbo, M.-H. *J. Chem. Phys.* **2003**, *118*, 29.
 (49) Navarro, R. In *Magnetic Properties of Layered Transition Metal Compounds*; de Jongh, L. J., Ed.; Kluwer Academic Publishers: Dordrecht, The Netherlands, 1990.

- (50) Canals, B. *Phys. Rev. B* **2002**, *65*, 184408.
 (51) Chen, J.-M.; Lin, K. Y. *Chin. J. Phys.* **2001**, *39*, 267.